Three-dimensional electron momentum densities of solids

2001 J. Phys.: Condens. Matter 13 7905

(http://iopscience.iop.org/0953-8984/13/34/327)

INSTITUTE OF PHYSICS PUBLISHING JOURNAL OF PHYSICS: CONDENSED MATTER

J. Phys.: Condens. Matter **13** (2001) 7905–7922 PII: S0953-8984(01)24205-2

Three-dimensional electron momentum densities of solids

F Bell[1] **and J R Schneider**[2]

[1] Sektion Physik, Universität München, Am Coulombwall 1, D-85748 Garching, Germany
[2] Hamburger Synchrotronstrahlungslabor (HASYLAB) at Deutsches Elektronen-Synchrotron (DESY), Notkestrasse 85, D-22603 Hamburg, Germany

Received 24 April 2001
Published 9 August 2001
Online at stacks.iop.org/JPhysCM/13/7905

Abstract

We report on the measurement of the three-dimensional electron momentum density (EMD) of solids by means of the (γ, eγ) reaction. Fixing the reaction kinematics by a coincidence condition, the triple-differential cross section for Compton scattering is proportional to the EMD. The experiments were performed either at the wiggler beamline of the European Synchrotron Radiation Facility (ESRF) or the undulator beamline of the PETRA storage ring at Deutsches Elektronen-Synchrotron (DESY) with photon energies of about 150 keV. Experimental three-dimensional EMDs of graphite, fullerene and aluminium are compared with theoretical ones obtained from band-structure calculations like the full-potential linear muffin-tin orbital, augmented-plane-wave and pseudopotential formulations. In addition, the change of the EMD caused by alloy formation has been studied in the Cu–Ni system and the results are compared with the Korringa–Kohn–Rostoker coherent potential approximation.

1. Introduction

The strong interest in the electronic structure of solids led to the development of a large variety of experimental methods for the study of energy dispersion and density of states both for occupied and unoccupied bands: photoemission spectroscopy [1], inelastic x-ray scattering [2], electron energy-loss spectroscopy [3], x-ray absorption spectroscopy [4], to name but a few. In contrast, few methods exist which measure directly wave-function-related quantities such as the real-space electron density (x-ray form factors) or momentum densities. These latter include the two-dimensional angular correlation of annihilation radiation (2D-ACAR) [5]—which, strictly speaking, measures the electron–positron pair density $\rho^{2\gamma}(\boldsymbol{p})$ [6]; see section 2—and (γ, eγ) and (e, 2e) spectroscopy [7]. (γ, eγ) experiments which are reviewed in this article are an extension of conventional Compton scattering where the double-differential cross section describing the energy and angular distribution of the scattered radiation is proportional to

the so-called Compton profile, which is defined as a twofold integration over the electron momentum distribution (EMD). This integration results from the lack of information about the momentum distribution of the recoiling electrons.

Since integration averages over large volumes in momentum space, detailed information about solid-state effects like Fermi surfaces or electron correlations might become difficult to obtain. It is therefore desirable to measure the EMD directly by fixing the complete scattering kinematics: if the momenta of the primary and scattered photon in addition to that of the recoil electron are measured simultaneously, i.e. in coincidence, the momentum of the electron in its initial state can be determined in a unique way. The corresponding triple-differential cross section is proportional to the EMD itself. (We mention that the 3D-EMD can also be obtained indirectly by means of non-coincident Compton scattering if a rather large number of directional Compton profiles are measured and finally reconstruction techniques based on Fourier transforms are employed [8].) The main difficulty of a $(\gamma, e\gamma)$ coincidence experiment originates in the strong incoherent elastic scattering of the recoiling electron within the target which disturbs the determination of the recoil momentum by causing multiple scattering. Since the mean free path for elastic scattering of electrons with recoil energies of tens of keV is only about 100 nm, self-supporting targets are required which are as thin as possible.

This has drastic implications for the coincident count rate: the mean free path for Compton scattering in carbon at a photon energy of 180 keV is 3 cm. Thus, in a 20 nm thin foil only one out of 10^6 photons will be scattered. To determine the photon and electron momenta, rather small solid angles of both the photon and electron detector are required. Assuming as a guess an isotropic angular distribution of the scattered photons, a solid angle of the photon detector of 10^{-4} srad yields another factor, 10^5. With a rather coarse angular resolution of the recoil momenta and a coincidence count rate of several Hz, we end up with a desired monochromatized photon flux of 10^{12} photons s^{-1} at the target. This flux at photon energies of about 180 keV can only be delivered by modern synchrotron radiation sources with large lepton energies. Thus, experiments have been performed at the high-energy x-ray scattering beamline ID15A of the ESRF (electron energy 6 GeV), which is equipped with an asymmetric wiggler with seven periods and strong magnetic poles of 1.8 T, and at the new undulator beamline at the PETRA storage ring (12 GeV) at DESY.

A method very similar to the $(\gamma, e\gamma)$ one is the (e, 2e) reaction where instead of a photon an energetic electron is used as projectile [9]. Again, multiple electron scattering within the target is the most severe problem. Comparing $(\gamma, e\gamma)$ and (e, 2e) experiments the situation is more 'relaxed' in the former case since at least the photon will not be multiply scattered. The advantage of the (e, 2e) technique is its large cross section and its monochromatic projectile flux. A highly monochromatic electron flux of 10^{12} electrons s^{-1} (100 nA) is easily achieved whereas comparable photon fluxes with considerably less monochromaticity are obtained only from synchrotron radiation facilities of the third generation. Altogether, this allows the introduction of electron spectrometers in (e, 2e) experiments which in turn makes it possible to measure the EMD of solids as a function of the valence binding energy with a resolution of about 1.5 eV [9].

2. Method

If a photon with energy ω and momentum $\boldsymbol{k}$ is scattered at an electron with binding energy $\epsilon > 0$ and momentum $\boldsymbol{p}$, energy and momentum conservation laws yield for these energies and momenta (we use atomic units)

$$\epsilon = \omega - \omega' - E' \tag{1}$$

$$\boldsymbol{p} = \boldsymbol{k}' + \boldsymbol{p}' - \boldsymbol{k} \tag{2}$$

where $(\omega', \boldsymbol{k}')$ and $(E', \boldsymbol{p}')$ are the energies and momenta of the photon and electron after the interaction. Thus, if $\boldsymbol{k}$, $\boldsymbol{k}'$ and $\boldsymbol{p}'$ are known experimentally, $\boldsymbol{p}$ can be determined in a unique way. For the coincident detection of both the scattered photon $(\omega', \boldsymbol{k}')$ and the recoil electron $(E', \boldsymbol{p}')$ the triple-differential cross section

$$\frac{\mathrm{d}^3\sigma}{\mathrm{d}\omega'\,\mathrm{d}\Omega_\gamma\,\mathrm{d}\Omega_\mathrm{e}} = \frac{\omega}{\omega'}p'\left(\frac{\mathrm{d}\sigma}{\mathrm{d}\Omega_\gamma}\right)_{KN}\rho(\boldsymbol{p}) \tag{3}$$

holds [10], where $\rho(\boldsymbol{p})$ is the EMD and $(\mathrm{d}\sigma/\mathrm{d}\Omega_\gamma)_{KN}$ the Klein–Nishina cross section for linearly polarized photons. The validity of the so-called impulse approximation is assumed.

Usually, the EMD for crystalline solids is obtained from a band-structure calculation. Due to translational invariance the corresponding wave functions are Bloch waves:

$$\phi_{\boldsymbol{k},i}(\boldsymbol{r}) = u_{\boldsymbol{k},i}(\boldsymbol{r})\mathrm{e}^{\mathrm{i}\boldsymbol{k}\cdot\boldsymbol{r}} \tag{4}$$

where the crystal momentum $\boldsymbol{k}$ is restricted to the first Brillouin zone and i is the band index. From the lattice periodicity of $u_{\boldsymbol{k},i}(\boldsymbol{r})$ it follows that

$$u_{\boldsymbol{k},i}(\boldsymbol{r}) = \sum_{\boldsymbol{g}} A_{\boldsymbol{g},i}(\boldsymbol{k})\mathrm{e}^{\mathrm{i}\boldsymbol{g}\cdot\boldsymbol{r}}. \tag{5}$$

Evaluating the Fourier transform $\phi_{\boldsymbol{k},i}(\boldsymbol{p})$ of equation (4) yields the EMD $\rho(\boldsymbol{p})$:

$$\rho(\boldsymbol{p}) = 2\sum_{\boldsymbol{k},\boldsymbol{g},i} n_i(\boldsymbol{k})\left|\phi_{\boldsymbol{k},i}(\boldsymbol{p})\right|^2 \tag{6}$$

or

$$\rho(\boldsymbol{p}) = 2\sum_{\boldsymbol{k},\boldsymbol{g},i} n_i(\boldsymbol{k})\left|A_{\boldsymbol{g},i}(\boldsymbol{k})\right|^2 \delta(\boldsymbol{p}-\boldsymbol{k}-\boldsymbol{g}). \tag{7}$$

$n_i(\boldsymbol{k})$ are the occupation number densities. Within the independent-particle model they are equal to unity for momenta smaller than the Fermi momentum and zero above. This holds for the reduced zone scheme. Non-diagonal elements n_{ij} of the occupation number density due to electron–electron interaction (equivalent to the configuration interaction in Hartree–Fock theory) are believed to be negligible, at least when the nearly-free-electron approximation is applicable [11]. For comparison we mention that the corresponding expression in the case of ACAR yields for the electron–positron pair density [12]

$$\rho^{2\gamma}(\boldsymbol{p}) = 2\sum_{\boldsymbol{k},\boldsymbol{g},i} n_i(\boldsymbol{k})\left|A^{+-}_{\boldsymbol{g},i}(\boldsymbol{k})\right|^2 \delta(\boldsymbol{p}-\boldsymbol{k}-\boldsymbol{g}) \tag{8}$$

where the Fourier components of the corresponding electron–positron Bloch state are given by

$$A^{+-}_{\boldsymbol{g},i}(\boldsymbol{k}) = \sum_{\boldsymbol{g}'} A^{+}_{\boldsymbol{g}'}(0)A^{-}_{\boldsymbol{g}-\boldsymbol{g}',i}(\boldsymbol{k}) \tag{9}$$

where A^- and A^+ are the separate Fourier components of the electron and positron wave function respectively. It is readily seen that except for a positron wave function $u^+_0(\boldsymbol{r}) =$ constant, i.e. $A^+_{\boldsymbol{g}} = \delta(\boldsymbol{g})$, the densities of equations (7) and (8) are different.

3. Experiment

The $(\gamma, \mathrm{e}\gamma)$ experiments were performed either at the high-energy x-ray undulator beamline of HASYLAB at the 12 GeV PETRA storage ring [13] or at the wiggler beamline ID15A of the 6 GeV storage ring of the ESRF [14]. Since the experimental set-ups are not very different we describe in the following that of the PETRA experiment only. The white photon beam was

monochromatized by a planar, slightly disordered Si crystal in the Laue geometry [15]. The disorder widens the rocking curve considerably compared to the Darwin width of a perfect crystal and matched the monochromaticity of the photon beam (width $\sigma_\omega = 0.35$ keV) with the energy resolution of the photon detector (see below) without a major loss of reflectivity. Thus, a photon flux of 2×10^{12} photons s^{-1} in a beam spot of 2×2 mm^2 could be reached at a photon energy of 180.3 keV and an average storage ring current of 30 mA. For photon detection we implemented a two-dimensional array of 12 intrinsic Ge diodes (energy resolution $\sigma_{\omega'} = 0.32$ keV) which was mounted externally to the evacuated target chamber at a scattering angle of $\theta = 150^\circ$ (figure 1).

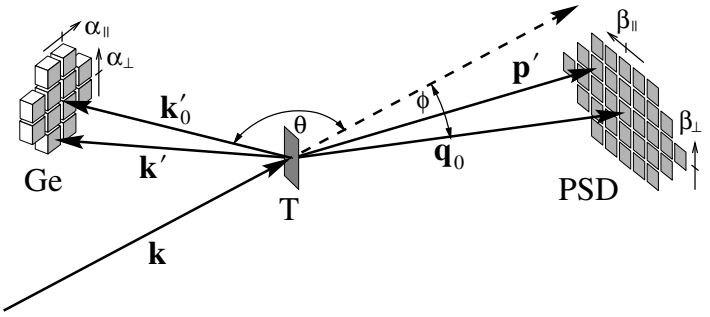

Figure 1. The experimental (γ, eγ) set-up: Ge, 12-pixel Ge diode; T, target; PSD, 32-pixel position-sensitive electron detector.

The unscattered photon beam was accurately dumped in a lead-shielded hollow body to minimize the x-ray background. The electrons were identified by a position-sensitive detector (PSD) consisting of a two-dimensional array of 32 individual PIN diodes. The detector arrays were set up in such a way that the vector $\boldsymbol{q}_0 = \boldsymbol{k} - \boldsymbol{k}'_0$, i.e., the momentum transfer to an electron initially at rest, was pointing at the centre of the PSD, while $\boldsymbol{k}'_0$, the momentum of the corresponding scattered photon, was defined by the centre of the Ge diode array. The surface normal of the target foils was parallel to $\boldsymbol{q}_0$. The final electron momentum p' is obtained from the energy conservation law of equation (1) by neglecting the binding energy ε which is small (tens of eV at most) compared to $\omega'_0 = 108.7$ keV, where ω'_0 is the photon energy after scattering from an electron at rest. A momentum transfer $q_0 = 75.0$ au guarantees the validity of the impulse approximation. The angle between $\boldsymbol{q}_0$ and $\boldsymbol{k}'_0$ (figure 1) is $\delta = \theta + \phi = 161.2^\circ$. We use a Cartesian coordinate system for the electron momentum $\boldsymbol{p}$ where the p_z-component is parallel to $\boldsymbol{q}_0$ and the p_x-component is lying in the ($\boldsymbol{k}$, $\boldsymbol{k}'_0$) scattering plane. In this coordinate system, the initial electron momentum components read

$$p_x = q_0\beta_\parallel - \left(\frac{\omega'_0}{c}\cos\delta\right)\alpha_\parallel + \left(\frac{1}{c}\sin\delta\right)\Delta\omega' \tag{10}$$

$$p_y = q_0\beta_\perp + \frac{\omega'_0}{c}\,\alpha_\perp \tag{11}$$

$$p_z = \left(\frac{\omega'_0}{c}\sin\delta\right)\alpha_\parallel - \frac{c\sin\delta}{\omega'_0\sin\theta}\,\Delta\omega' \tag{12}$$

where $\alpha_{\parallel,\perp}$ and $\beta_{\parallel,\perp}$ are the angular deviations of $\boldsymbol{k}'$ from $\boldsymbol{k}'_0$ and $\boldsymbol{p}'$ from $\boldsymbol{q}_0$ respectively (figure 1) and $\Delta\omega' = \omega' - \omega'_0$ is the photon Doppler broadening. Each detector channel in the photon and electron branch was provided with an independent pre-amplifier and main amplifier and discriminator. The pre-amplified photon signals were processed by a spectroscopy

amplifier delivering a fast and slow output signal. The discriminated fast signal served as a gate for the coincidence unit; the amplitude of the slow signal was used for the measurement of the final photon energy ω'. If the coincidence unit detected a discriminated electron signal within the open gate, the complete data sets of both the coincidence unit and the ADC were read out via a VME bus.

Detailed Monte Carlo (MC) simulations of the momentum resolution $R(p_x, p_y, p_z)$ of the $(\gamma, e\gamma)$ spectrometer included the correlated scattering due to the triple-differential cross section of equation (3), solid angles and energy resolution of the Ge diodes, energy broadening of the primary photon beam and the extended beam spot at the target. Since the photon energy resolution particularly influences both the p_x- and p_z-resolution (see equations (10)–(12)), they are not independent of each other. The surfaces R = constant are to a good approximation ellipsoids with principal axes which, due to this dependence, are rotated away from the Cartesian coordinate system by a small angle. Thus, we fitted a trivariate Gaussian to the MC simulation, and from the diagonal elements of the resulting covariance matrix we obtained the standard deviations $(\sigma_{xx}, \sigma_{yy}, \sigma_{zz}) = (0.14, 0.14, 0.27)$ au and non-vanishing off-diagonal elements $\sigma^2_{xz} = \sigma^2_{zx} = -7.4 \times 10^{-3}$ au^2 leading to a small anti-correlation. Whenever in the following the experiment is compared with theory, the latter has been folded with the trivariate Gaussian described above.

4. Results and discussion

4.1. Graphite

The mean free path for 70 keV recoil electrons in graphite is 90 nm [16], which requires thin target foils to suppress multiple scattering. They were made either by laser plasma ablation (lpa) or by thermal evaporation (te). In the former case pure graphite was irradiated by a 30 GW cm^{-2} Nd:YAG laser for about 10 ns [17, 18]. The ablated single C atoms with an average energy of a few eV were collected on a thin betaine film which had a fine crystalline-like structure that acted as a replica for the graphite film and guaranteed a high mechanical stability. The te-foils were made by evaporation of graphite heated to about 3200 K. At such moderate temperatures the evaporated species are not monatomic but carbon clusters of different sizes [19]. These clusters are fragments of the (002) planes and leave the graphite surface with thermal energies of about 0.3 eV [17]. Impinging on the surface of the substrate, they do not have sufficient kinetic energy to break the molecular bonds. Again, the evaporated material was condensed on a betaine film which was finally dissolved in water and the self-supporting lpa- or te-foils were mounted on a stainless steel frame. The thicknesses of the films were determined by light transmission and were 17 nm for the lpa-foil and 18 nm for the te-foil. The mounted foils were finally laser annealed: the te-foil at 4200 K for about 10 ns [20] and the lpa-foil for 30 μs at about 3000 K [18]. Transmission electron microscopy revealed a complete graphitization of the foils and that the average length L_a of the basal planes was increased from less than 1 nm immediately after condensation to about 10 nm by this treatment. Foils which had been prepared under identical conditions have been extensively investigated by means of either high-resolution electron microscopy (HREM) or electron diffraction (ED) with 80 keV electrons [20]. While for the lpa-foil all low-index rings of graphite can be observed and their intensity pattern indicates an isotropic distribution of crystallites [18, 20], the (002) ring is missing in the case of the te-foil. Since diffraction angles are small for 80 keV electrons ($\Theta_{002} = 6.2$ mrad) the lack of this ring implies that (002) planes cannot lie more or less perpendicular to the foil surface. ED patterns from the edge of a folded foil where the surface was nearly parallel to the electron beam developed (002) rings. This clearly demonstrates

that for te-foils the basal planes were arranged mostly parallel to the foil surface, repeating in essence the results of Klein [21] on evaporated carbon films.

In the following, experimental EMDs will be compared with theoretical ones obtained from band-structure calculations [22]. To do that, the experimental data have been normalized to an effective number of electrons by integrating both experiment and theory over the same volume in momentum space which is determined by experimental conditions. Theoretical EMDs are based on either an empirical pseudopotential (PP) method [23] with potential parameters from Reed *et al* [24], the full-potential linear muffin-tin orbital (FP-LMTO) [25] or the modified augmented-plane-wave (MAPW) method [26]. All calculations were performed within the general scheme of density functional theory (DFT). In the FP-LMTO method non-overlapping muffin-tin spheres are introduced and the electron potential and the charge density are expanded in spherical harmonics inside the spheres and Fourier transformed in the interstitial region. In the present calculation, 2410 plane waves were used for the representation of the charge density and the potential in the interstitial region. 250 $(\boldsymbol{k}+\boldsymbol{g})$ terms were used in the Fourier sums. 77 $\boldsymbol{k}$-points were produced by division of the irreducible Brillouin zone. After self-consistency of the electron potential and the charge density had been achieved, the angular averaging of the EMD was performed. In the MAPW scheme the electron potential is assumed to be of warped-muffin-tin form, e.g., spherically symmetric within the non-overlapping (APW) spheres centred at each C atom and described by a superposition of plane waves outside the spheres. In the whole atomic cell each Bloch function is expressed by a superposition of up to 364 plane waves and is augmented inside the APW spheres by properly chosen solutions of the radial differential equation with the spherically symmetric potential. Both the wave functions as well as their first derivatives are exactly continuous at the surface of the APW spheres [27]. This guarantees the rapid decay of the Fourier transform of the Bloch functions. The MAPW

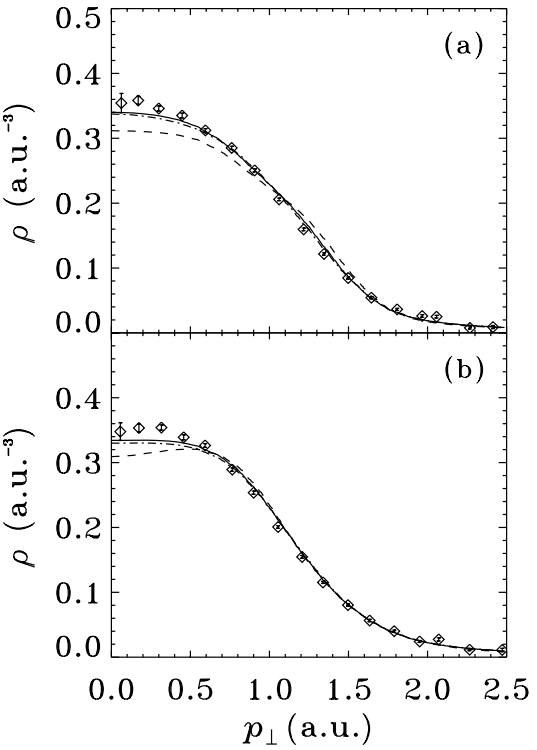

Figure 2. The EMD for the te-foil (a) and the lpa-foil (b) as functions of $p_\perp$ at $p_\parallel = 0$. PP: broken line; FP-LMTO: solid line; MAPW: dash–dotted line.

scheme is an all-electron method which treats the core and valence electrons on an equal footing. Due to the structure of the foils observed by means of ED, the theoretical EMDs have been either spherically averaged to represent the lpa-targets or azimuthally averaged in the case of the te-foil. The momentum component parallel to the c-axis is called $p_\parallel = p_z$, the component within the basal plane $p_\perp = \sqrt{(p_x^2 + p_y^2)}$. Electron multiple scattering has been taken into account by convoluting theoretical EMDs with elastic scattering distributions obtained from Monte Carlo simulations [7,28]. This procedure has been applied for all comparisons between experiment and theory reported in this review.

To allow a quantitative comparison, the following figures show one-dimensional cuts through the EMDs. Figures 2(a) and 2(b) show $\rho(p_\perp, p_\parallel = 0)$ for the te- and lpa-foils respectively. Data points are compared with PP (broken curve), FP-LMTO (solid curve) and MAPW (dash–dotted curve) calculations. Evidently, FP-LMTO and MAPW calculations (with a slight tendency of the MAPW calculations to be superior to FP-LMTO calculations in the case of the lpa-foil) describe the data better than PP calculations, a fact which has also been recognized by Metz *et al* [28]. But we also observe that the often-cited deficiency of a PP calculation of not reproducing the wave-function oscillations near the nuclei and therefore of underestimating the EMD at large momenta [29] is not significant for the comparison with our data. The discrepancy between our data and PP results is not due to an underestimation of high-momentum components—and therefore a reduction of intensity at small momenta due to charge conservation—but due to different slopes for experiment and theory. On the other hand, non-coincident Compton scattering experiments also revealed that the PP calculations by Reed *et al* [24] tend to overestimate momentum anisotropies [30, 31]. In figure 3, $\rho(p_\perp = 0, p_\parallel)$

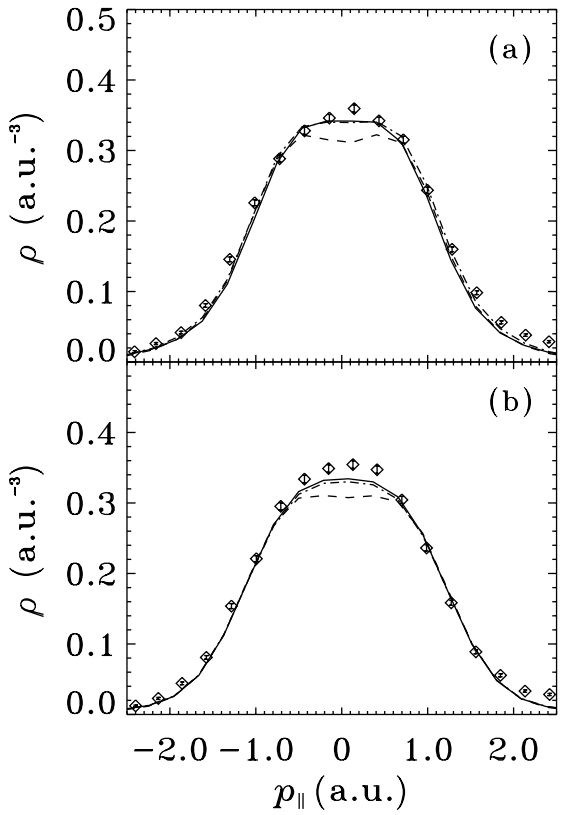

Figure 3. The EMD for the te-foil (a) and the lpa-foil (b) as functions of $p_\parallel$ at $p_\perp = 0$. PP: broken line; FP-LMTO: solid line; MAPW: dash–dotted line.

is compared with theory for the te-foil (figure 3(a)) and the lpa-foil (figure 3(b)). Whereas the FP-LMTO and MAPW calculations clearly describe the data better at small momenta, the PP calculation is slightly superior at larger momenta, though the effect is not strong enough to favour the PP description within the uncertainty of our data. The sequence of theories, compared with experiment and shown by the 1D cuts of figures 2 and 3, is also supported by the global fits of the complete 3D-EMD: the normalized χ^2/n (n: number of bins) is 2.15 (MAPW), 3.07 (FP-LMTO) and 3.80 (PP) in the case of the te-foil, and 2.22 (MAPW), 2.40 (FP-LMTO) and 2.71 (PP) for the lpa-foil.

Figure 4 shows the difference of the EMDs from te- and lpa-foils $\Delta\rho(p_\perp = \text{constant}, p_\parallel)$ for $p_\perp = 0.0$ au (figure 4(a)), $p_\perp = 0.9$ au (figure 4(b)), $p_\perp = 1.3$ au (figure 4(c)) and $p_\perp = 1.5$ au (figure 4(d)). Though the error bars are rather large, the minimum at $p_\parallel = 0$ is better described by FP-LMTO and MAPW calculations than by the PP calculation. In

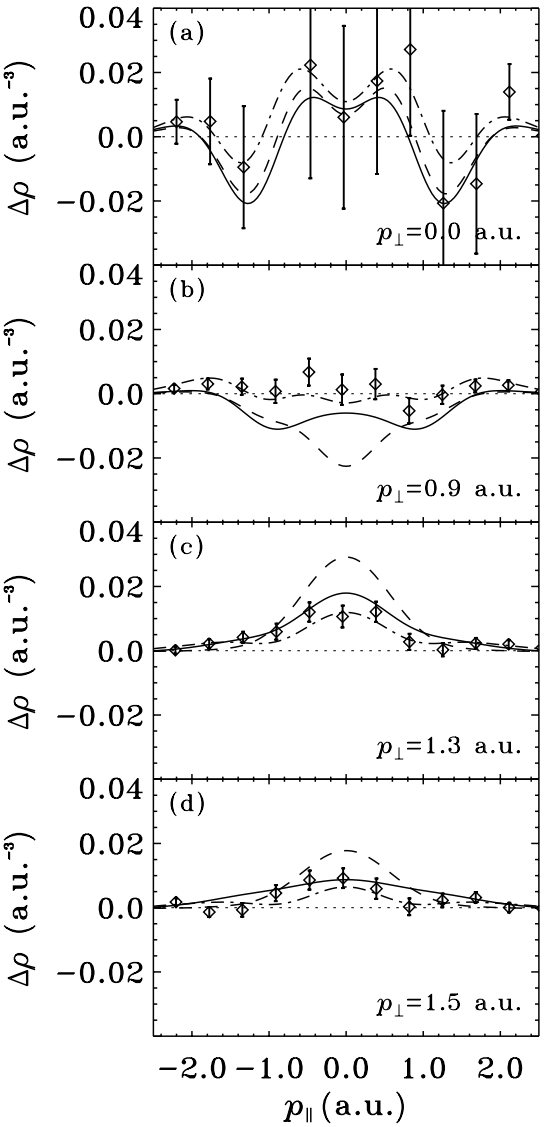

Figure 4. The difference $\Delta\rho$: the EMD of the te-foil minus that of the lpa-foil, as a function of $p_\parallel$ for different values of $p_\perp$. PP: broken line; FP-LMTO: solid line; MAPW: dash–dotted line.

figure 5 the differences of the EMDs from te- and lpa-foils are plotted as functions of the electron momentum $p_\perp$ in the basal plane for $p_\parallel = 0.3$ au (figure 5(a)), $p_\parallel = -0.1$ au (figure 5(b)), $p_\parallel = -1.0$ au (figure 5(c)) and $p_\parallel = -1.4$ au (figure 5(d)). Experimental data are compared again with PP (broken curve), FP-LMTO (solid curve) and MAPW (dash–dotted curve) calculations. Again, the anisotropy is better reproduced by the FP-LMTO and MAPW calculations than the PP one. We mention that the PP calculation of Lou *et al* [23] also failed to describe the non-coincident Compton scattering experiment on pyrolytic graphite of Manninen *et al* [32]. A more qualitative demonstration of the anisotropy of the graphite EMD is shown in figure 6(a) where contour lines of the difference of the theoretical EMDs, i.e., basal averaged minus spherically averaged EMD, are plotted as functions of $p_\perp$ and $p_\parallel$. Figure 6(b) shows the influence of resolution and electron multiple scattering on this difference. Evidently, the strength of the anisotropies is reduced, but the general structure is retained. In figure 6(c) the

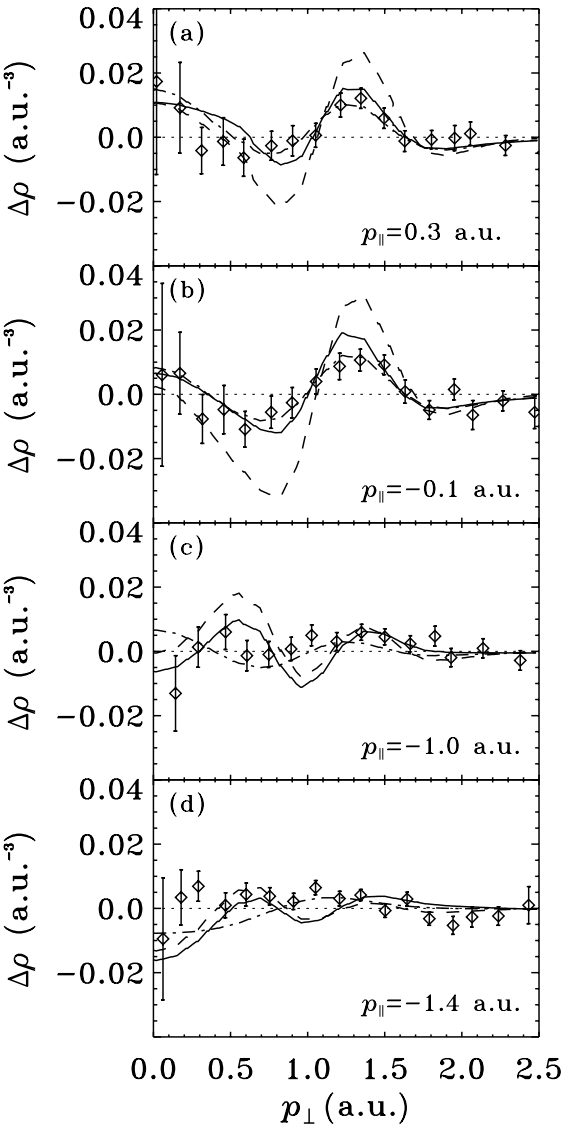

Figure 5. The difference $\Delta\rho$: the EMD of the te-foil minus that of the lpa-foil, as a function of $p_\perp$ for different values of $p_\parallel$. PP: broken line; FP-LMTO: solid line; MAPW: dash–dotted line.

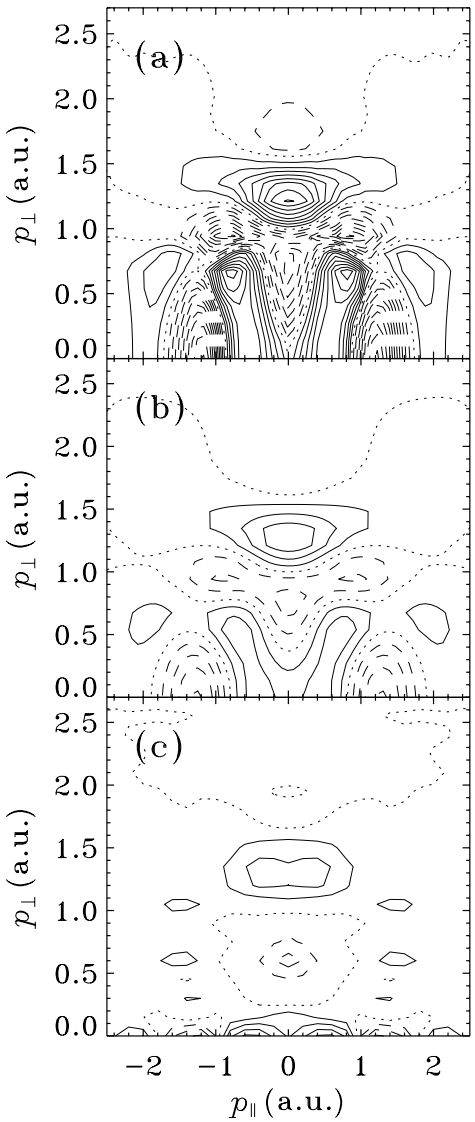

Figure 6. The azimuthally minus the spherically averaged EMD. Solid lines represent a positive difference, dashed lines a negative one, and the dotted line indicates zero difference. The theoretical FP-LMTO difference (a), the theoretical difference corrected for experimental resolution and electron multiple scattering (b) and the experimental difference (c). The latter has been symmetrized with respect to $p_\parallel = 0$. The difference between the lines is 0.005 au^{-3} in each case.

experimental difference is plotted and should be compared with the theoretical difference of figure 6(b). The comparison reveals that the general features of the experimental anisotropies are reproduced by theory.

4.2. Fullerene

The most remarkable difference between the EMDs of graphite and C_{60} is the increased density of C_{60} compared to graphite at small momenta [28]. The bending of the graphite basal planes to form the buckyball induces a hybridization of wave functions with s character with those of the π-electrons, which results in a charge transfer from the interlayer region into the shell of the C_{60} spheres [33, 34]. (Nevertheless, bonding is closer to the sp^2 hybrids of graphite than to the sp^3 bonding in diamond [35].) Consequently, a DFT calculation in the local

density approximation (LDA) revealed that the electron density for most of the 120 bands in fullerene showed a larger overlap among the nearest-neighbour carbon atoms in the C_{60} ball compared to graphite [36]. This kind of delocalization results apparently in an enhancement of the EMD at small momenta. A comparison of one-dimensional cuts through the EMD of fullerene with either the FP-LMTO calculation for graphite or the molecular C_{60} calculation showed that experiment could not distinguish between the two theories within error bars [28]. To improve the statistics we have summed up all coincidence events for a constant p_z-value. The resulting coincident Compton profile $J_{coinc}(p_z)$ is not identical to a non-coincident one due to the limited integration range in the p_x- and p_y-directions which results from the finite extent of the electron detector, but besides the increase in statistics it also has the advantage that measurements in coincidence provide photon spectra free from any background radiation. Again, experimental J_{coinc} have been normalized to the effective number of electrons given by the restricted range of momenta. Figure 7 shows the experimental J_{coinc} as a function of p_z (data points) together with the corresponding molecular fullerite calculation [28]. The agreement is at the per cent level. To enlarge possible differences, we have plotted in figure 8 the relative difference $\Delta J_{coinc} = [(J_{exp} - J_{theor})/J_{exp}] \times 100$ where J_{exp} is the experimental coincident Compton profile and J_{theor} the corresponding theoretical profile, i.e. the theoretical EMD has been integrated over the limited (p_x, p_y) range mentioned above. Open circles are from the FP-LMTO calculation for graphite; full circles represent the molecular C_{60} calculation. Though the relative difference is rather small, experiment clearly favours the C_{60} calculation. Figure 8 also demonstrates the above-mentioned momentum transfer towards smaller momenta if C_{60} is formed from graphene sheets: due to norm conservation this is reflected by $J_{exp}(C_{60}) < J_{theor}(\text{graphite})$ for large momenta.

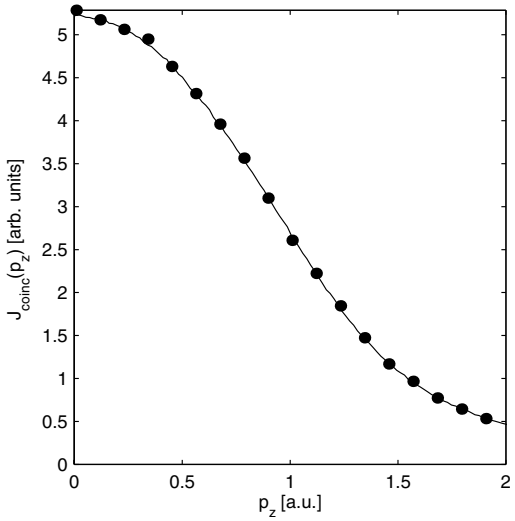

Figure 7. The experimental coincident Compton profile J_{coinc} (dots) compared to the molecular C_{60} calculation.

4.3. Aluminium

A comparison between the experimental EMD and results from band-structure calculations has been made. In essence, the Fourier components $A_{g,i}(\boldsymbol{k})$ of equation (5) have been calculated by the linear muffin-tin orbital method either in the atomic sphere (ASA-LMTO) [37] or the

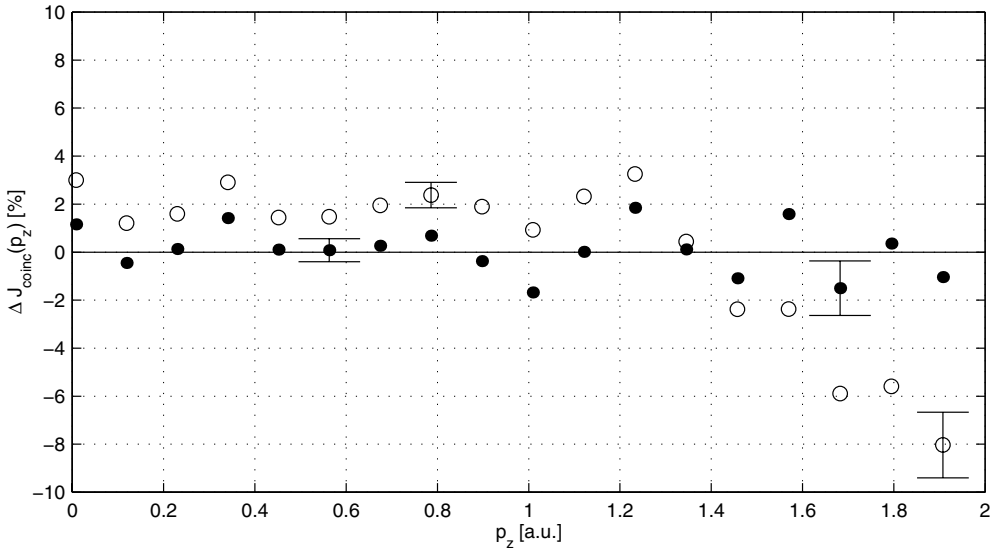

Figure 8. The relative difference ΔJ_{coinc} for the FP-LMTO calculation for graphite (open circles) and the C_{60} calculation (dots).

full-potential approximation (FP-LMTO) [25]. In the ASA-LMTO calculation a unit cell of the crystal is substituted for with a number of overlapping atomic spheres with no room left for the interstitial region. The electron potential is assumed to be spherically symmetric inside the spheres. In the FP-LMTO calculation a number of non-overlapping muffin-tin spheres are introduced; the potential is expanded in spherical harmonics inside the spheres and Fourier transformed in the interstitial region. This treatment of the interstitial region provides superior accuracy at the price of increasing computation time.

2D or 3D EMDs of aluminium have been measured in the past both by the ACAR [5,38] and by the (e, 2e) technique [9,39,40]. For comparison with 2D-ACAR data we have evaluated from our results the angular correlation density [41]

$$\rho^{2D}(p_x, p_y) = \int \rho(p_x, p_y, p_z)\, \mathrm{d}p_z \tag{13}$$

which is plotted in figure 9 together with 2D-ACAR from reference [38]. It is readily seen that in the ACAR data the EMD is cut-off at $p_x = p_y \cong 1$ au due to the positron wave function being repelled from the ion core. Recent calculations by Alatalo *et al* [42] show a drastic reduction of the positron wave function in aluminium for distances below 2 au in real space. This in turn means that high-momentum components A_g^+ in equation (9) strongly influence the electron–positron pair density $\rho^{2\gamma}$. Nothing like that happens in the $(\gamma, \mathrm{e}\gamma)$ experiment which shows appreciable intensity beyond 1 au due to the core states.

If all the events for a constant p_z-value are summed up we obtain again a coincident Compton profile J_{coinc}, a procedure which increases the statistics considerably. Due to the limited range of our experiment in the p_x- and p_y-directions, the contribution of core states to J_{coinc} is strongly reduced if compared with a non-coincident Compton profile. In figure 10 we compare J_{coinc} with theory: the dash–dotted curve is from ASA-LMTO calculation, and the dotted curve results from FP-LMTO calculation, demonstrating that FP-LMTO calculation agrees better with experiments than ASA-LMTO calculation. This seems to point to a general problem if EMDs are obtained from Fourier-transformed wave functions which have been

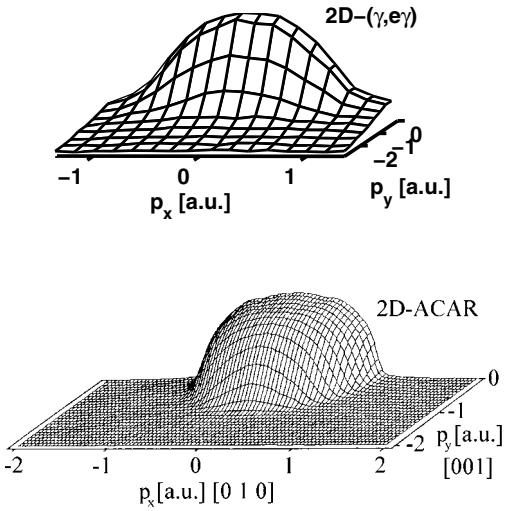

Figure 9. 2D angular correlation plots for $(\gamma, e\gamma)$ and ACAR measurements [38].

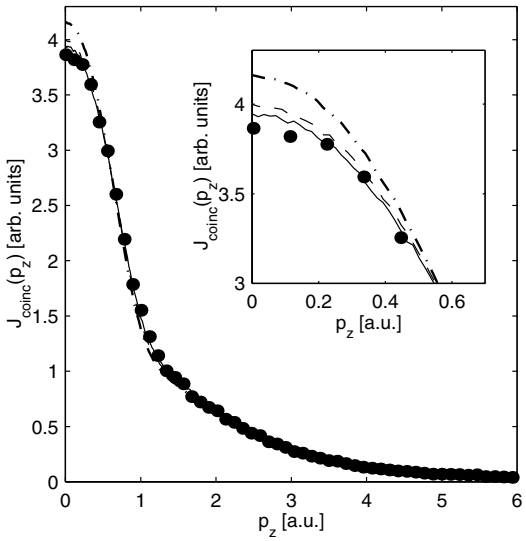

Figure 10. The coincident Compton profile J_{coinc}. Dots: experiment (the dot size represents the statistical uncertainty); dash–dotted line: ASA-LMTO approximation; dashed line: FP-LMTO approximation; solid line: FP-LMTO approximation including the LP correction. The inset shows the curves at low momenta on an enlarged scale.

calculated within the framework of DFT. It has been shown by Lam and Platzman [43] that the EMD obtained from the Kohn–Sham (KS) orbitals should be augmented by a functional derivative $\delta E_c[n]/\delta\epsilon_p$ of the total correlation energy $E_c[n]$ with respect to the free-particle energies ϵ_p. Thus, the correction accounts for correlations between KS orbitals. This becomes more transparent if discussed in connection with the homogeneous electron gas. In that case, the KS electrons are not interacting moving in a constant effective potential, and therefore the KS orbitals are simply plane waves. The EMD is the step function of the non-interacting electron gas with no occupied states above the Fermi momentum p_F though the Fermi energy

itself is corrected for the self-energy [44], which, in the DFT-LDA, is given by the exchange–correlation potential [45]. Application of the above-mentioned correction changes the EMD to that of the interacting gas where due to electron–electron interaction quasiparticle states are populated above p_F. The solid curve in figure 10 incorporates in addition to the FP-LMTO correction this Lam–Platzman (LP) correction. The LP correction further improves the agreement between experiment and theory. We have also calculated the LP correction for graphite and fullerene but it is vanishingly small for these cases. We mention that the band structures for the occupied states from the two theories a very similar. Differences—including those of bandwidths and gaps—are at the mRyd level and would thus be hardly detectable on an absolute scale, e.g. by angle-resolved photoemission experiments [1]. Though the EMDs of the two theories also differ by a few per cent only, this effect can be detected by means of Compton scattering unambiguously.

4.4. Cu–Ni alloy

In this section we will report on the influence of alloying by comparing the EMD of $Cu_{0.50}Ni_{0.50}$ with those of its pure constituents [46]. The electronic structure of this 3d transition-metal solid-solution alloy has received extensive attention. The Cu–Ni system is completely soluble over the whole concentration range, i.e. there is no miscibility gap yielding single-phase disordered fcc alloys. Substantial improvement has been achieved in the theoretical understanding of the electronic structure of disordered alloys using a general multiple-scattering formalism. Three principal approximations have been investigated:

(i) the virtual-crystal approximation (VCA), where the effective potential of the alloy is the average of those of the pure constituents,
(ii) an average t-matrix approximation (ATA) and
(iii) the coherent potential approximation (CPA), where a self-consistency requirement is introduced to obtain the single-site t-matrix [47,48]. It is this property of the CPA which makes it preferable to apply, especially for alloys of high concentrations.

The underlying Green's function technique of the multiple-scattering problem is similar to that of the Korringa–Kohn–Rostoker theory (KKR) [49,50]. Bansil and co-workers [51,52] have extensively investigated the Cu–Ni system theoretically. On the experimental side, polycrystalline Cu_xNi_{1-x} alloys have been investigated by means of conventional Compton scattering [53] and the CPs were compared with those from KKR-CPA calculations. Qualitative agreement was found, though at small momenta the influence of alloying was predicted by theory to be stronger than that revealed by experiment.

Since self-supporting Cu or Ni foils with diameters of 8 mm and thicknesses of 20 nm cannot be prepared, we have evaporated 22 nm Cu followed by 22 nm Ni onto a 30 nm thin C foil acting as a backing. The backing was made by condensation of evaporated carbon atoms on a thin betaine film which was finally dissolved in water, and the carbon film was mounted on a frame. Both Cu and Ni were evaporated on the free-standing carbon backing at rates of about 0.5 nm s^{-1}, and the films condensed at room temperature. In order not to lose beam time by using the heating procedure, we decided to prepare two sandwich foils simultaneously, where the second was heated at about 500 °C for 2 h and then furnace cooled. The data of Almazouzi *et al* [54] yield a diffusion coefficient of about $D = 2 \times 10^{-19}$ m^2 s^{-1} giving for a heating time of $t = 7 \times 10^3$ s a diffusion length $x = 2\sqrt{Dt} = 80$ nm. This is four times the Cu (or Ni) thickness. That an alloy has in fact been formed by this heat treatment was confirmed by x-ray diffraction (XD) experiments either made with the sandwich or the annealed specimen. Figure 11 shows the (111) reflections of Cu and Ni in the case of the

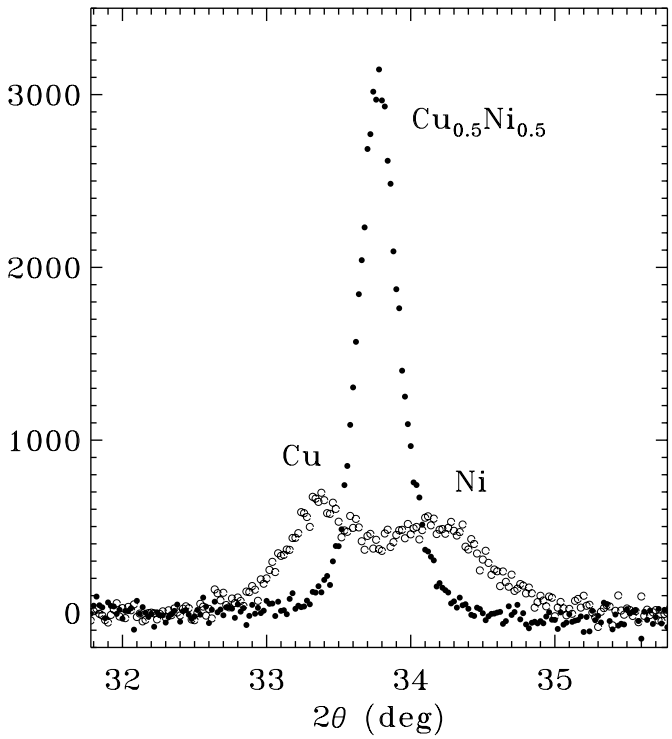

Figure 11. The (111) reflections of the sandwich foil (open circles) and the heat-treated foil (filled circles).

sandwich (open circles) or the (111) reflection (filled circles) of the alloy in the case of the heat-treated film. Since the lattice parameter of the alloys changes almost linearly between those of the constituents [55], the measurement reveals that within the experimental uncertainty a 50:50 alloy has been formed.

To improve the statistics we have summed up all events for a constant p_z to obtain a coincident Compton profile J_{coinc}, which has been evaluated in absolute units by normalizing it to the effective number $Z_{\rm eff}$ of electrons contributing to it. Figure 12 shows the difference $\Delta J = J_{coinc}(\text{sandwich}) - J_{coinc}(\text{alloy})$ as a function of p_z (stars). As mentioned above, we used two different foils; one was untreated, the other was heat treated. If the difference between the measurements is attributed to the influence of alloying, one has to assume that the two foils are almost identical with regard to the sandwich composition and the backing. To remove any doubts, we later repeated the experiment with *one* foil only; first, measurements were made, then it was heat treated and, finally, measurements were made again. The result is shown by the filled circles in figure 12; it demonstrates the reliability of the two-foil experiment. Due to improved statistics, an alloying effect is clearly observable. At $p_z = 0$ it amounts to about 2% of the total coincident profile, i.e. it is a rather small effect. We compare in figure 12 also with the experimental non-coincident CP difference $\Delta J = (J_{\rm Cu} + J_{\rm Ni})/2 - J_{\rm Cu_{0.5}Ni_{0.5}}$ [53]. Despite the oscillations, the general trend of the experimental points (open circles) agrees nicely with our results. The oscillatory behaviour might be an artifact introduced by the numerical procedure of data processing [53]. Neither data processing such as a deconvolution procedure accompanied by frequency filtering nor background subtraction has been applied to our data. This might be viewed in the light of a remark made by Bansil *et al* [56] that in their

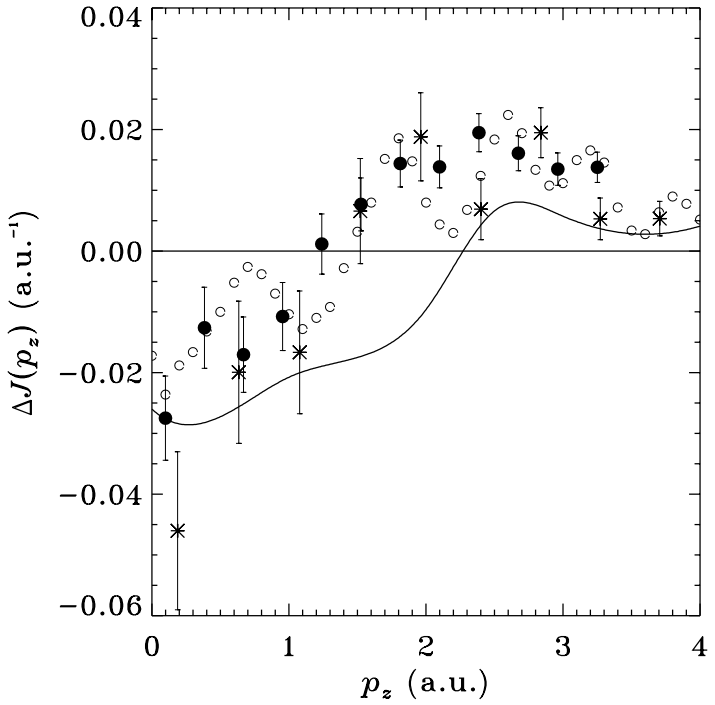

Figure 12. The coincident Compton profile (CP) difference (stars and filled circles) and the non-coincident CP of reference [53] (open circles). The solid curve represents KKR-CPA theory [53].

non-coincident Compton scattering experiments on Cu–Ni single crystals, absolute values of experimental CPs are difficult to interpret due to the presence of a background contribution of uncertain origin. The solid line in figure 12 represents KKR-CPA theory [46, 53]. In view of the smallness of the effect, a reasonable agreement between theory and experiment is observed. We emphasize that both experiment and theory are on an absolute scale in figure 12.

The use of ultrathin target foils, in particular, opens up the possibility of studying a large class of random binary alloys that are produced far from thermodynamic equilibrium. Instead of producing the alloys by interdiffusion, they could be made either by simultaneous evaporation and condensation of the constituents or by co-sputtering. In this way arbitrary alloy compositions are achieved that would otherwise be impossible to get from the melt. On the other hand, KKR-CPA calculations are independent of thermodynamic conditions.

5. Summary

We have shown that by coincident detection of the scattered x-ray photon and its recoil electron, the complete 3D electron momentum density of solids can be measured. Examples for graphite, fullerene and aluminium are given and the experimental EMDs are compared with theoretical ones obtained from band-structure calculations. In the case of graphite, FP-LMTO and MAPW results describe the experimental EMD better than a pseudopotential calculation. For fullerenes the bending of graphene sheets to form a buckyball changes the EMD in a characteristic way which is revealed by experiment. The Fourier transforms of the density functional wave functions are not really the wave functions in momentum space. Thus the EMD should be corrected, an effect first noticed by Lam and Platzman [43]. For aluminium this correction

could be verified. The influence of alloying on the EMD was studied in the Cu–Ni system and the results are in satisfactory agreement with a KKR-CPA theory.

Finally, it might be appropriate to comment on non-coincident Compton scattering work, which nowadays is usually high-resolution Compton spectroscopy based on Bragg spectrometers. If directional Compton profiles (CP) are compared with theory, the situation seems to be somewhat confusing: whereas in the cases of Be [57] and Al [58] almost perfect agreement is achieved, for materials like Li, Na [59, 60], Si [61] or Cu [62], deviations up to 15% are observed. It is not obvious whether theory or experiment is responsible for this discrepancy [61]. Due to this uncertainty, there seems to be a tendency to emphasize more differences of directional CPs—or power spectra respectively [63,64]—and derivatives of CPs which are especially sensitive to features of the Fermi topology (fermiology). We also mention that due to rather low incident x-ray energies (10 keV), typical in high-resolution experiments, doubts arose about the validity of the impulse approximation due to strong electron–hole interaction in the final state [65].

Acknowledgments

We are indebted to our colleagues who contributed over the years to these investigations: F Kurp, C Metz, A J Rollason, T Sattler and Th Tschentscher. We wish to thank A S Kheifets and H Bross who provided their band-structure calculations to us and H Ehrenberg for help with the XD experiment. This work was supported by the German Federal Ministry of Education and Research, Contract Nos 055WMAAI and 05ST8HRA.

References

[1] Levinson H, Greuter F and Plummer E 1983 *Phys. Rev.* B **27** 727
[2] Schülke W, Schulte-Schrepping H and Schmitz J 1993 *Phys. Rev.* B **47** 12 426
[3] Fink J 1992 *Unoccupied Electronic States* vol 69, ed J Fuggle and J Inglesfield (Berlin: Springer)
[4] Batra I and Kleinman L 1984 *J. Electron. Spectrosc. Relat. Phenom.* **33** 175
[5] Mader J, Berko S, Krakauer H and Bansil A 1976 *Phys. Rev. Lett.* **37** 1232
[6] Puska M and Nieminen R 1994 *Rev. Mod. Phys.* **66** 841
[7] Kurp F, Vos M, Tschentscher Th, Kheifets A S, Schneider J R, Weigold E and Bell F 1997 *Phys. Rev.* B **55** 5440
[8] Schülke W, Stutz G, Wohlert F and Kaprolat A 1996 *Phys. Rev.* B **54** 12 381
[9] Canney S, Vos M, Kheifets A S, Clisby N, McCarthy I E and Weigold E 1997 *J. Phys.: Condens. Matter* **9** 1931
[10] Bell F, Tschentscher T, Schneider J and Rollason A 1991 *J. Phys. B: At. Mol. Opt. Phys.* **24** L533
[11] Lundqvist B and Lydén C 1971 *Phys. Rev.* B **4** 3360
[12] Berko S 1983 *Positron Solid-State Physics (Proc. Int. 'Enrico Fermi' School of Physics, course 83)* ed W Brandt and A Dupasquier (Amsterdam: North-Holland)
[13] Hahn U, Schulte-Schrepping H, Balewski K, Schneider J R, Ilinski P, Lai B, Yun W, Legnini D and Gluskin E 1997 *J. Synchrotron Radiat.* **4** 1
[14] Suortti P and Tschentscher Th 1995 *Rev. Sci. Instrum.* **66** 1798
[15] Schneider J R, Gonçalves O D, Rollason A J, Bonse U, Lauer J and Zulehner W 1988 *Nucl. Instrum. Methods* B **29** 661
[16] Mayol R and Salvat F 1997 *At. Data Nucl. Data Tables* **65** 55
[17] Dollinger G and Maier-Komor P 1991 *Nucl. Instrum. Methods* A **303** 50
[18] Dollinger G, Frey C M and Maier-Komor P 1993 *Nucl. Instrum. Methods* A **334** 167
[19] Drowart J, Burns R P, Maria G and Inghram G 1959 *J. Chem. Phys.* **31** 1131
[20] Dollinger G, Maier-Komor P and Mitwalsky A 1991 *Nucl. Instrum. Methods* A **303** 79
[21] Klein C A 1962 *J. Appl. Phys.* **33** 3338
[22] Sattler T, Tschentscher Th, Schneider J R, Vos M, Kheifets A S, Lun D R, Weigold E, Dollinger G, Bross H and Bell F 2001 *Phys. Rev.* B **63** 155204
[23] Lou Y, Johansson B and Nieminen R M 1991 *J. Phys.: Condens. Matter* **3** 1699
[24] Reed W A, Eisenberger P, Pandey K C and Snyder L C 1974 *Phys. Rev.* B **10** 1507

[25] Kheifets A S, Lun D R and Savrasov S Yu 1999 *J. Phys.: Condens. Matter* **11** 6779
[26] Bross H, Bohn G, Meister G, Schubö W and Stöhr H 1970 *Phys. Rev.* B **2** 3098
[27] Roth-Seefried H and Bross H 1977 *Z. Phys.* B **26** 125
[28] Metz C, Tschentscher Th, Suortti P, Kheifets A S, Lun D R, Sattler T, Schneider J R and Bell F 1999 *J. Phys.: Condens. Matter* **11** 3933
[29] Chou M Y, Cohen M L and Louie S G 1986 *Phys. Rev.* B **33** 6619
[30] Tyk R, Felsteiner J, Gertner I and Moreh R 1985 *Phys. Rev.* B **32** 2625
[31] Loupias G, Chomilier J and Guérard D 1984 *J. Physique Lett.* **45** L301
[32] Manninen S, Honkimäki V and Sourtti P 1993 *Z. Naturf.* a **48** 295
[33] Haddon R C 1992 *Acc. Chem. Res.* **25** 127
[34] Troullier N and Martins J L 1992 *Phys. Rev.* B **46** 1754
[35] Taylor R and Walton D R M 1993 *Nature* **363** 685
[36] Moscovici J, Loupias G, Rabii S, Erwin S, Rassat A and Fabre C 1995 *Europhys. Lett.* **31** 87
[37] Skriver H 1984 *The LMTO Method* (Berlin: Springer)
[38] Berko S, Haghgooie M and Mader J 1977 *Phys. Lett.* A **63** 335
[39] Hayes P, Williams J and Flexman J 1991 *Phys. Rev.* B **43** 1928
[40] Canney S, Kheifets A, Vos M and Weigold E 1998 *J. Electron. Spectrosc. Relat. Phenom.* **88–91** 247
[41] Metz C, Tschentscher Th, Suortti R, Kheifets A S, Lun D R, Sattler T, Schneider J R and Bell F 1999 *Phys. Rev.* B **59** 10 512
[42] Alatalo M, Barbiellini B, Hakala M, Kauppinen H, Korhonen T, Puska M J, Saarinen K, Hautojärvi P and Nieminen R M 1996 *Phys. Rev.* B **54** 2397
[43] Lam L and Platzman P 1974 *Phys. Rev.* B **9** 5122
[44] Kohn W and Sham L J 1965 *Phys. Rev.* **140** A1133
[45] Sánchez-Friera P and Godby R W 2000 *Phys. Rev. Lett.* **85** 5611
[46] Metz C, Tschentscher Th, Sattler T, Höppner K, Schneider J R, Wittmaack K, Frischke D and Bell F 1999 *Phys. Rev.* B **60** 14 049
[47] Bansil A 1993 *Z. Naturf.* a **48** 165
[48] Bansil A 1987 *Electronic Band Structure and its Applications (Springer Lecture Notes Series vol 283)* edited M Yussouff (Heidelberg: Springer) p 273
[49] Korringa J 1947 *Physica* **13** 391
[50] Kohn W and Rostoker N 1954 *Phys. Rev.* **94** 1111
[51] Bansil A 1979 *Phys. Rev.* B **20** 4035
[52] Bansil A, Rao R S, Mijnarends P E and Schwartz L 1981 *Phys. Rev.* B **23** 3608
[53] Benedek R, Prasad R, Manninen S, Sharma B K, Bansil A and Mijnarends P E 1985 *Phys. Rev.* B **32** 7650
[54] Almazouzi A, Macht M P, Naundorf V and Neumann E 1996 *Phys. Rev.* B **54** 857
[55] Coles B R 1956 *J. Inst. Met.* **84** 346
[56] Bansil A, Kaprzyk S, Andrejczuk A, Dobrzynski L, Kwiatkowska J, Maniawski F and Zukowski E 1998 *Phys. Rev.* B **57** 314
[57] Huotari S, Hämäläinen K, Manninen S, Kaprzyk S, Bansil A, Caliebe W, Buslaps T, Honkimäki V and Suortti P 2000 *Phys. Rev.* B **62** 7956
[58] Suortti P, Buslaps T, Honkimäki V, Metz C, Shukla A, Tschentscher Th, Kwiatkowska J, Maniawski F, Bansil A, Kaprzyk S, Kheifets A S, Lun D R, Sattler T, Schneider J R and Bell F 2000 *J. Phys. Chem. Solids* **61** 397
[59] Kubo Y 1997 *J. Phys. Soc. Japan* **66** 2236
[60] Sakurai Y, Tanaka Y, Bansil A, Kaprzyk S, Stewart A T, Nagashima Y, Hyodo T, Nanao S, Kawata H and Shiotani N 1995 *Phys. Rev. Lett.* **74** 2252
[61] Kralik B, Delaney P and Louie S G 1998 *Phys. Rev. Lett.* **80** 4253
[62] Sakurai Y, Kaprzyk S, Bansil A, Tanaka Y, Stutz G, Kawata H and Shiotani N 1999 *J. Phys. Chem. Solids* **60** 905
[63] Isaacs E D, Shukla A, Platzman P M, Hamann D R, Barbiellini B and Tulk C A 1999 *Phys. Rev. Lett.* **82** 600
[64] Shukla A, Barbiellini B, Erb A, Manuel A, Buslaps Th, Honkimäki V and Suortti P 1999 *Phys. Rev.* B **59** 12 127
[65] Sternemann C, Hämäläinen K, Kaprolat A, Soininen A, Döring G, Kao C-C, Manninen S and Schülke W 2000 *Phys. Rev.* B **62** R7687